

1 Various lithospheric deformation patterns derived from 2 rheological contrasts between continental terranes: 3 Insights from 2-D numerical simulations

4 Renxian Xie^{1,2}, Lin Chen³, Jason P. Morgan², Yongshun John Chen^{2*}

5 ¹School of Transportation Engineering, East China Jiaotong University, Nanchang, 330013, China

6 ²Department of Ocean Science and Engineering, Southern University of Science and Technology,
7 Shenzhen, 518055, China

8 ³State Key Laboratory of Lithospheric Evolution, Institute of Geology and Geophysics, Chinese
9 Academy of Sciences, Beijing, 100029, China

10 *Correspondence to:* Yongshun John Chen (johnyc@sustech.edu.cn)

11 **Abstract.** Continents are formed by the amalgamation of numerous micro-terranes and island arcs, so
12 they have spatially varying lithosphere strengths. The Crème brûlée (CB) model and the Jelly sandwich
13 (JS) model have been commonly used to describe continental lithosphere strength-depth variations.
14 Depending on the strength of continental lower crust, the CB and JS models can be further subdivided
15 into two subclasses, in which the I subclass (CB-I and JS-I) and II subclass (CB-II and JS-II)
16 respectively have a strong or weak lower crust. During continental collision, lithosphere deformation is
17 the byproduct of the comprehensive interaction of multiple terranes. Here we used 2-D
18 thermo-mechanical numerical models that contain three continental terranes to systematically explore
19 the effects of terranes with various strengths on continental deformation, and studied the effects of
20 different rheological assumptions on terrane deformation. We found four types of lithosphere
21 deformation patterns: collision, subduction, thickening and delamination, and replacement. These
22 simulation patterns are seen in observed deformation patterns and structures in East Asia, suggesting
23 they are likely to be naturally occurring modes of intracontinental orogenesis.

24 1. Introduction

25 Continents have undergone multiple break-up and assembly events during the past ~2 billion years,
26 with the assembly events often being associated with the accretion and deformation of numerous
27 micro-terranes (Mitchell et al., 2021). Accreted terranes have different ages ranging from ~3500 – 3000
28 Ma to 50 – 0 Ma, and diverse compositions and structures linked to their diverse continental, arc, or

29 oceanic origin, which often leads to them having distinct initial lithospheric thicknesses and strengths
30 (Artemieva, 2006; Audet and Bürgmann, 2011; Pasyanos et al., 2014; Morgan and Vannucchi, 2022).
31 The lithosphere of ancient continental terranes like cratons are usually thick and strong, while younger
32 lithosphere of continental margins and tectonically active regions is thin and weak (Audet and
33 Bürgmann, 2011; Burov, 2011), and deeply buried former oceanic fragments can have temperature and
34 strengths that vary over ~ 0.5 Gyr timescale (Morgan and Vannucchi, 2022).

35 Continental lithosphere strength conventionally been represented by two prevailing rheology models
36 —the Crème brûlée (CB) and the Jelly sandwich (JS) idealizations (Chen and Molnar, 1983; Jackson,
37 2002; Burov and Watts, 2006; Bürgmann and Dresen, 2008; Burov, 2011). The Crème brûlée scenario
38 suggests that lithosphere strength resides entirely in the crust, with the lithospheric mantle being much
39 weaker (with this strength contrast being the explanation for why little seismicity is typically seen in
40 the continental mantle, despite rock-mechanics arguments that it should usually be stronger than its
41 overlying crust). In contrast, the Jelly sandwich model is based on conventional rock mechanics
42 arguments which imply that in general the continental middle and lower crust should be weaker than
43 overlying cooler upper crust and underlying further-from-solidus lithospheric mantle (Figure 1a). The
44 rheology of the continental lower crust can also differ strongly in different continental terranes due to
45 the varieties in composition, temperature, water content, stress, and tectonic environment (Bürgmann
46 and Dresen, 2008; Hacker et al., 2015; Morgan and Vannucchi, 2022). Therefore, the CB and JS
47 conceptualizations can be further subdivided into CB-I and CB-II, JS-I, and JS-II subclasses that reflect
48 potentially variable strengths of the lower crust: CB-I and JS-I, CB-II and JS-II have strong and weak
49 continental lower crust, respectively (Fig. 1a). Observations in Eastern Asia show a wide variability in
50 terrane deformation styles that argue for the potential feasibility of all four of these rheological models
51 (Figure 1b).

52 Several previous numerical modelling studies have discussed the effects of rheological contrasts
53 between terranes in lithosphere deformation in a collisional system. Studies containing two terranes
54 have explored contrasts in crustal rheology, and found that this can greatly change the morphology, size
55 and deep lithosphere structure of collisional orogenic belt (Chen, 2021; Chen et al., 2017; Cook and
56 Royden, 2008; Faccenda et al., 2008; Sun and Liu, 2018; Vogt et al., 2018; Xie et al., 2021). Strong
57 crust also has the potential to protect its underlying lithospheric mantle from deformation and
58 destruction (Heron and Pysklywec, 2016). Studies containing three or more terranes in their models

59 have usually focused on the middle terrane which can play a crucial role in lithosphere deformation in a
60 collisional system (Kelly et al., 2016, 2020; Li et al., 2016; Huangfu et al., 2018, 2022; Sun and Liu,
61 2018; Xie et al., 2023). A weak middle terrane is easy to be thickened, to the point where eventually its
62 lithospheric mantle can be delaminated from the crust; while a moderate-strength middle terrane can
63 induce far-field orogenesis; and a strong middle terrane may prevent propagation of deformation and
64 facilitate underthrusting of the advancing terrane. In addition, some studies have also stressed the
65 importance of local pre-existing weak zones which can change the order and style of lithosphere
66 deformation (Chen et al., 2020; Heron et al., 2016; Sokoutis and Willingshofer, 2011; Xie et al., 2021).
67 Large-scale continental collisional system often involves the multiple units of an indenting terrane, a
68 middle terrane, and far-end backwall terranes. These terranes have different lithosphere rheologies and
69 thicknesses, and they collectively contribute to several styles of continental deformation (Artemieva,
70 2006; Audet and Bürgmann, 2011; Pasyanos et al., 2014; Morgan and Vannucchi, 2022). Here, we use a
71 2-D thermo-mechanical numerical modeling method to systematically study the effects of terranes with
72 various rheological properties on continental deformation. Our numerical models simulate a
73 continent-continent collisional system that contains three continental terranes. They explore the effects
74 of four groups of lithosphere deformation patterns linked to the four rheological idealizations of CB-I,
75 CB-II, JS-I, and JS-II applied to each terrane. We will summarize the rheological features for each
76 deformation pattern, and then apply the simulations to better understand ongoing and past deformation
77 histories of various orogenic belts in eastern Asia, such as the eastern Tien Shan orogenic belt, the
78 Tibetan Plateau and the Early Paleozoic Orogen in Southeastern China.

79 **2. Numerical modelling method and model setup**

80 **2.1. Numerical modelling method**

81 Our thermo-mechanical models were performed with the I2VIS code of Gerya and Yuen (2003a),
82 previously used in Xie et al. (2021, 2023). This code combines finite differences with marker-in-cell
83 techniques to solve the mass, momentum, and energy conservation equations for incompressible flow.
84 It incorporates the non-Newtonian visco-plastic rheologies for the lithosphere, as well as the possibility
85 to include parameterizations of the effects of surface processes like sedimentation and erosion.

86 **2.1.1. Governing equations**

87 The mass conservation equation for incompressible flow is:

$$88 \quad \frac{\partial v_x}{\partial x} + \frac{\partial v_y}{\partial y} = 0, \quad (1)$$

89 The momentum conservation equations (Stokes equations) are:

$$90 \quad \begin{aligned} \frac{\partial \sigma'_{xx}}{\partial x} + \frac{\partial \sigma'_{xy}}{\partial y} &= \frac{\partial P}{\partial x}, \\ \frac{\partial \sigma'_{yy}}{\partial y} + \frac{\partial \sigma'_{xy}}{\partial x} &= \frac{\partial P}{\partial y} - g\rho \end{aligned} \quad (2)$$

91 The energy (heat) conservation equation is:

$$92 \quad \begin{aligned} \rho C_p \frac{DT}{Dt} &= -\frac{\partial q_x}{\partial x} - \frac{\partial q_y}{\partial y} + H_r + H_s + H_a + H_L \\ q_x &= -k \frac{\partial T}{\partial x} \\ q_y &= -k \frac{\partial T}{\partial y} \\ H_a &= T\alpha \frac{DP}{Dt} \\ H_s &= \sigma'_{xx} \dot{\epsilon}_{xx} + \sigma'_{yy} \dot{\epsilon}_{yy} + 2\sigma'_{xy} \dot{\epsilon}_{xy} \end{aligned} \quad (3)$$

93 where x and y represent the horizontal and vertical coordinate directions, and v_x and v_y are the
 94 corresponding velocity components, respectively. σ'_{ij} and $\dot{\epsilon}_{ij}$ ($i, j = x, y$) are deviatoric stress and
 95 strain-rate tensors, respectively; g is the gravitational acceleration; ρ is density. In the heat conservation
 96 equation, q_x and q_y are the horizontal and vertical components of the heat flux, respectively; C_p is heat
 97 capacity, and H_r , H_a , H_s , and H_L denote the radioactive, adiabatic, shear, and latent heat production,
 98 respectively; k is the thermal conductivity.

99 The rheological constitutive relationship connects the deviatoric stress and strain rate:

$$100 \quad \begin{aligned} \sigma'_{xx} &= 2\eta_{eff} \dot{\epsilon}_{xx}, \quad \dot{\epsilon}_{xx} = \frac{\partial v_x}{\partial x} \\ \sigma'_{xy} &= 2\eta_{eff} \dot{\epsilon}_{xy}, \quad \dot{\epsilon}_{xy} = \frac{1}{2} \left(\frac{\partial v_x}{\partial y} + \frac{\partial v_y}{\partial x} \right), \\ \sigma'_{yy} &= 2\eta_{eff} \dot{\epsilon}_{yy}, \quad \dot{\epsilon}_{yy} = \frac{\partial v_y}{\partial y} \end{aligned} \quad (4)$$

101 where η_{eff} is the effective viscosity.

102 2.1.2. Rheology

103 Here we make the conventional assumption that the crust and mantle have a visco-plastic rheology.

104 Viscous deformation is determined as a combination of diffusion and dislocation creep that depends on

105 temperature, pressure, and strain rate, expressed as (Gerya, 2019):

$$\begin{aligned} \eta_{disl} &= \frac{1}{2} \frac{1}{(A_D)^{-1/n} (\dot{\epsilon}_D)^{(n-1)/n}} \exp\left(\frac{E_a + V_a P}{nRT}\right) * S \\ \eta_{diff} &= \frac{1}{2} \frac{A_D}{\sigma_{cr}^{(n-1)}} \exp\left(\frac{E_a + V_a P}{RT}\right) * S \end{aligned} \quad (5)$$

107 For mineral aggregates, both dislocation and diffusion creep occur simultaneously, with a combined

108 effective viscosity given by:

$$\frac{1}{\eta_{ductile}} = \frac{1}{\eta_{disl}} + \frac{1}{\eta_{diff}}, \quad (6)$$

110 where η_{disl} and η_{diff} are viscosities for dislocation and diffusion creep, respectively. σ_{cr} is the

111 critical stress for the dislocation to diffusion stress transition, and the parameters A_D , E_a , V_a , and n are a

112 material constant, activation energy, activation volume, and stress exponent, respectively, and R is the

113 universal gas constant. The strength scaling factor, S , is introduced as a simple parameter to vary the

114 lithospheric viscosity.

115 Plasticity is implemented using a conventional pseudo-viscous yield criterion first used to study rifting

116 (e.g. Chen and Morgan, 1990) that is extended to include a strain-weakening-like parameterization of

117 fracture-related strain weakening (Gerya et al., 2010; Vogt et al., 2017):

$$\eta_{plastic} = \frac{\sigma_{yield}}{2\dot{\epsilon}_{II}}$$

$$\sigma_{yield} = C + P\phi$$

$$118 \quad C = \begin{cases} C_a + (C_b - C_a) \times \frac{\gamma}{\gamma_{cr}}, & \text{if } \gamma \leq \gamma_{cr} \\ C_b, & \text{if } \gamma \geq \gamma_{cr} \end{cases}, \quad (7)$$

$$\phi = \begin{cases} \phi_a + (\phi_b - \phi_a) \times \frac{\gamma}{\gamma_{cr}}, & \text{if } \gamma \leq \gamma_{cr} \\ \phi_b, & \text{if } \gamma \geq \gamma_{cr} \end{cases}$$

119 where σ_{yield} is yield stress, P is dynamic pressure, γ is the integrated plastic strain, and γ_{cr} is the
 120 upper strain limit for fracture-related weakening. C and ϕ are cohesion and friction angle that depend
 121 on the plastic value. C_a and ϕ_a are the initial and C_b and ϕ_b are final strength values, respectively.
 122 This involves making the rheological assumption that deeply percolating fluids and high pore fluid
 123 pressures can significantly lower the plastic strength of fractured rocks.
 124 The final effective viscosity is determined by the minimum value between the ductile and plastic
 125 viscosities (Ranalli, 1995):

$$126 \quad \eta_{eff} = \min(\eta_{ductile}, \eta_{plastic}). \quad (8)$$

127 2.1.3. Surface processes

128 Topography in our models evolves according to a transport equation that is solved at each time step,
 129 with a crude local parameterization of effects of accounts for sedimentation and erosion:

$$130 \quad \frac{\partial y_{es}}{\partial t} = v_y - v_x \frac{\partial y_{es}}{\partial x} - v_s + v_e. \quad (9)$$

131 Where y_{es} is the vertical position of the surface as a function of horizontal distance x ; and v_x and v_y are
 132 the corresponding velocity components, respectively. v_s and v_e are the sedimentation and erosion rates,
 133 respectively, conforming to the relation:

$$134 \quad v_s = 0 \text{ mm/yr}, v_e = 0.3 \text{ mm/yr when } y_{es} > 5 \text{ km};$$

$$135 \quad v_s = 0.3 \text{ mm/yr}, v_e = 0 \text{ mm/yr when } y_{es} < 5 \text{ km}.$$

136 Owing to surface processes are not our focuses in this study, for the aim of simplification, we adopt a
 137 small erosion and sedimentation rates of 0.3 mm/yr, which are similar to previous studies (Gerya and

138 Yuan, 2003b; Bian et al., 2020). As well, we simply choose a very large value of 5 km as the threshold
139 for initiating denudation and sedimentation to further weaken the influences of surface processes on the
140 evolutions of our model.

141 **2.2. Model Setup**

142 The 2-D numerical model covers a rectangular computational domain of 3000 km × 700 km and
143 consists of 1360 × 400 non-uniform grid cells with dozens of mobile markers in each grid cell to
144 transport physical properties (Figure 2a). Above 300 km, the cell-size of the grid in the middle of
145 model ($X = 1300 - 2200$ km) is 1 km × 1 km, and gradually widens towards the two sides to finally
146 become 5 km × 1 km. From the 300 km depth to the model bottom, each grid is stretched to 5 km in the
147 vertical direction. As a result, the grid in the middle of the model ($X = 1300 - 2200$ km) is 1 km × 5 km
148 and is 5 km × 5 km in the other regions. Changing resolutions in different model regions can ensure the
149 model can finely depict lithosphere deformation in the region of interest while improving the
150 calculation's efficiency.

151 In the initial configuration, the model comprises three continental terranes — the Pro-, Mid- and
152 Retro-terrane — which refer to the indenting 'Pro-' terrane driven by plate convergence, an
153 intermediate 'Mid-' terrane, and a far-end backwall 'Retro-' terrane, respectively (Figure 2a). For the
154 purpose of simplification, the three terranes are assumed to have the same initial crustal structure with
155 20 km thick upper and lower crust, respectively. In the meanwhile, to simulate lateral structure
156 differences within continental lithosphere (Pasyanos et al., 2014), thicknesses of the initial lithospheric
157 mantle of the Pro-, Mid- and Retro-terrane are 160 km, 90 km, and 120 km, respectively. The rest of
158 the region is filled by asthenosphere except along the model top, where a 20 km thick layer of "sticky
159 air" with low viscosity (1×10^{18} Pas) and low density (1 kg/m^3) is placed to simulate the effects of a
160 free surface (Schmeling et al., 2008). Flow laws and material properties for each lithospheric layer are
161 listed in Table 1.

162 Mechanical boundary conditions of the model are that the top and sides are free-slip boundaries which
163 mean that the vertical velocity at the top boundary and horizontal velocity at the side boundaries are all
164 zero. The bottom is assumed to be a somewhat non-physical 'permeable boundary' that was developed
165 to reduce the required depth of the computational region (Burg and Gerya, 2005). For top-driven flows
166 like those considered here, this approximation has been shown to not affect deformation in the upper

167 parts of the region (Burg and Gerya, 2005). Finally, a constant convergence rate of 20 mm/yr is
168 assigned to the Pro-terranes ($X = 1000$ km) to drive the model.

169 Initial temperature conditions are set as follows: the model top is set to 0°C , the two side boundaries
170 are adiabatic boundaries with zero horizontal heat fluxes, and the model bottom has an initial
171 temperature of 1593°C , and can dynamically adjust as the model evolves. The initial thermal gradient
172 in the crust is $15^{\circ}\text{C}/\text{km}$ in the three terranes, so their Moho temperature is 600°C . A temperature of
173 1330°C is applied at the bottom of the lithospheric mantle of the three terranes, which leads to the Pro-
174 and Mid-terranes having minimum and maximal thermal gradients in the lithospheric mantle,
175 respectively (see the right plane in Figure 2a). An adiabatic thermal gradient of $0.5^{\circ}\text{C}/\text{km}$ is assumed
176 within the asthenosphere. The temperature field would evolve over time, thus, although the three
177 terranes are not in thermal equilibrium at the start of the experiments, it has few effects on model
178 evolution. The initial setup of lithosphere structure and temperature field make the Mid-terranes weakest
179 when same rheology model is used for the three terranes.

180 **3. Simulation Results**

181 The rheological models of CB-I, CB-II, JS-I, and JS-II result from different strength scaling factors for
182 the upper crust, the lower crust, and the lithospheric mantle in our numerical models (Figure 2b). We
183 systematically test the effects of these rheological assumptions on the deformation of the Pro-, Mid-
184 and Retro-terranes. According to different behaviors of lithosphere deformation, these simulation
185 results can be categorized into four basic modes of collision, subduction, thickening and delamination,
186 and replacement (Figures S1 and S2). In the deformation mode of collision, the lithospheric mantle of
187 the Mid-terranes is extruded out and the lithospheric mantles of the two bounding terranes meet and
188 collide together. In the deformation mode of subduction, the lithospheric mantle of one of the bounding
189 terranes subducts into the deep mantle below the Mid-terranes while the other one keeps almost
190 undeformed. In the deformation mode of thickening and delamination, one of the bounding terranes is
191 shortened by compression, and delamination may come on the heels of thickening of lithosphere due to
192 gravitational instability in some cases. In the deformation mode of replacement, the bottom of weak
193 and thick lithospheric mantle of the bounding terrane is scraped off by the strong lithospheric mantle of
194 the Mid-terranes, and replaced by the latter. Here, we select a typical case for each mode of lithosphere

195 deformation to describe more details of these modes of model evolution.

196 **3.1. Case 1: Lithosphere Collision**

197 Case 1 represents the scenario of lithosphere collision (Figure 3). In this model, the assumed
198 rheological models for the Pro-, Mid- and Retro-terrane are JS-I, JS-II, and JS-I, respectively, which
199 means that the Mid-terrane has a significantly weaker lower crust relative to the Pro- and
200 Retro-terrane. The lithospheric mantle of the Mid-terrane is also slightly weaker due to its thinner
201 lithosphere and correspondingly higher initial temperature field. The lithosphere strength profiles of the
202 three terranes are shown in Figure 3g.

203 The Mid-terrane is the first to deform when the Pro-terrane begins to collide, absorbing plate
204 convergence in the form of lithosphere thickening (Figures 3a and 3d). The upper crust of the
205 Mid-terrane breaks due to strain weakening, and several reverse faults are formed to absorb crustal
206 shortening. The lower crust folds, and strain diffusely distributes within it. Since the Retro-terrane is
207 relatively strong, it prevents crustal deformation from propagating into this terrane, and restricts the
208 bulk of deformation to the Mid-terrane. With continuous advance of the Pro-terrane and resistance of
209 the Retro-terrane, the crust of the Mid-terrane is intensively shortened, leading to more thrusting
210 structures in the upper crust and a “flower-like” structure in the lower crust (Figures 3b and 3e). Thrust
211 structures and crustal deformation also expand toward the Pro- and Retro-terrane at this stage.
212 Topography also grows towards the two bounding terranes (Figure 7a). Ultimately, the weak
213 lithospheric mantle of the Mid-terrane is squeezed out, and the Pro- and Retro-terrane's lithospheric
214 mantles meet and so start to collide beneath the overlying crust of the Mid-terrane (Figures 3c and 3f).

215 **3.2. Case 2: Lithosphere Subduction**

216 Case 2 shows lithosphere subduction of the Pro-terrane (Figure 4). In this model, the assumed
217 rheological models for the Pro-, Mid- and Retro-terrane are JS-II, JS-I, and JS-I, respectively. The
218 Mid-terrane has a stronger lower crust compared with the Pro-terrane, but its lithospheric mantle is a
219 little weaker than the Pro-terrane due to higher temperature field resulting from its thinner lithosphere
220 structure (Figure 4g). When convergence begins, the weak lower crust of the Pro-terrane is blocked by
221 the stronger lower crust of the Mid-terrane. This induces it to stack in a collisional front to form a
222 remarkable folding structure (Figures 4a and 4d). The strong lithospheric mantle of the Pro-terrane

223 continues to move forward and underthrusts beneath the Mid-terrane. As the Pro-terrane advances, its
224 crust gradually enters the Mid-terrane, inducing shortening and thickening of the upper crust of the
225 Mid-terrane, while the strong lower crust of the Mid-terrane almost keeps undeformed (Figures 4b and
226 4e).

227 Meanwhile, the lithospheric mantle of the Pro-terrane continues to underthrust scraping off part of the
228 lithospheric mantle of the Mid-terrane. Eventually, the crust of the Pro-terrane wedges a long distance
229 into the Mid-terrane, and the lithospheric mantle of the Pro-terrane subducts into the deeper mantle
230 (Figures 4d and 4f). In this example, crustal deformation and topography gradually propagate from the
231 Pro-terrane to the Mid-terrane, whereas the Retro-terrane remains nominally ‘undeformed’ at all times
232 (Figure 7b). In some experiments, the lithospheric mantle of the Retro-terrane can subduct beneath the
233 Mid-terrane (Figure S1).

234 **3.3. Case 3: Lithosphere Thickening and Delamination**

235 Case 3 illustrates the thickening and delamination of the lithospheric mantle of the Pro-terrane (Figure
236 5). In this case, the rheological models for the Pro-, Mid- and Retro-terrane are CB-II, JS-I, and JS-I,
237 respectively (Figure 5j). The Pro-terrane has a rheologically weaker lower crust and lithospheric mantle,
238 making it relatively easy to deform once the collision has started. The lithosphere of the Pro-terrane is
239 first thickened, and the crust starts to fold in two discrete zones (Figures 5a and 5f). The lower part of
240 the thickened lithospheric mantle is denser than its ambient mantle owing to lower temperature, which
241 causes it to drip downwards (Figures 5b–5h). After delamination of the thickened lithosphere,
242 subduction of the Pro-terrane’s lithospheric mantle along one of the deformation localization zones
243 absorbs the plate convergence (Figures 5e and 5i). Crustal deformation is restricted in the Pro-terrane
244 until lithosphere delamination, after which crustal strain and topography rapidly spread from the
245 Pro-terrane to the Mid-terrane (Figure 7c). Like case 2, the Retro-terrane stays essentially undeformed
246 at all times.

247 **3.4. Case 4: Lithosphere Replacement**

248 Case 4 illustrates how the lithospheric mantle of the Pro-terrane is replaced by that of a neighboring
249 stronger Mid-terrane (Figure 6). In this case, the rheological models for the Pro-, Mid- and
250 Retro-terrane are CB-I, JS-II, and JS-I, respectively. The Pro-terrane has a strong lower crust and a

251 thick and weak lithospheric mantle, while the Mid-terrane has a weaker lower crust and a strong
252 lithospheric mantle (Figure 6g). This lithosphere configuration between the Pro- and the Mid-terrane
253 causes deformation to be primarily distributed in the Pro-terrane's lithospheric mantle and the
254 Mid-terrane's crust. As a result, the Mid-terrane's crust becomes intensely shortened by fold and thrust
255 structures, but its strong lithospheric mantle wedges into the Pro-terrane's thick and weak lithospheric
256 mantle (Figures 6a, 6b, 6d and 6e). The strong lithospheric mantle of the Mid-terrane scrapes off the
257 lower part of the weak lithospheric mantle of the Pro-terrane and so replaces it (Figures 6c and 6f).
258 Similar to case 1, crustal deformation and topography expand from the Mid-terrane towards its side
259 terranes (Figure 7d). The lithospheric mantle of the Retro-terrane can also be replaced in some cases
260 (e.g. Figure S1).

261 **4. Discussion**

262 **4.1. Rheological Characteristics for Distinct Lithosphere Deformation Patterns**

263 Distinct lithosphere deformation patterns in our simulations arise from rheological contrasts between
264 neighboring continental terranes. Figure 8 summarizes the rheological characteristics of these distinct
265 deformation patterns. When the Mid-terrane's lithospheric mantle is weakest (typified by models in
266 which the rheological model of the Mid-terrane is CB-II), it is easy for its mantle to be extruded out,
267 leading to collision between the lithospheric mantles of its surrounding Pro- and Retro-terranes. When
268 one of the two bounding terranes has extremely weak lithospheric mantle, its lithosphere is first to be
269 thickened by compression, and delamination may follow due to density-driven instability. When the
270 lower crust of the Mid-terrane is relatively strong (CB-I or JS-I), while the lower crust is weaker in the
271 Pro- or Retro-terrane (CB-II or JS-II), the lithospheric mantle of the Pro- or Retro-terrane will tend to
272 subduct into the deep mantle, e.g. leading to intracontinental subduction. Finally, when the Mid-terrane
273 has a weak lower crust and strong lithospheric mantle (JS-II), while the Pro- or Retro-terrane has a
274 strong lower crust and weak lithospheric mantle (CB-I), the lithospheric mantle of the former may
275 replace the lithospheric mantle of the latter.

276 When the deformation patterns involve the collision and replacement of lithosphere, continental
277 deformation involves all three terranes (Figures 3 and 6). In contrast, the other deformation patterns
278 only involve two terranes, the Pro- or Retro-terrane and the Mid-terrane (Figures 4 and 5). The

279 rheological properties of the Mid-terrane are responsible for these differences. Like previous numerical
280 studies (Kelly et al., 2016, 2020; Li et al., 2016; Huangfu et al., 2018, 2022; Sun and Liu, 2018), our
281 simulations show that a weak Mid-terrane is easier to deform, and that in this case lithosphere
282 deformation will expand from center to its neighboring sides; while a relatively strong Mid-terrane
283 prevents deformation from propagating far, so that lithosphere deformation is constrained to occur
284 within two terranes..

285 Although our multi-terrane numerical models mainly focus on the impact of the lateral strength
286 differences between different terranes in a continental collisional system, rheological models of CB-I,
287 CB-II, JS-I, JS-II also involve vertical rheological variation (Figure 1a). It seems difficult to summarize
288 how vertical strength variation affects lithosphere deformation of the continental collisional system.
289 For example, in some cases, only changing the rheological models of the Pro- or Retro-terranes may
290 produce distinct deformation modes such as collision, subduction, thickening and delamination, and
291 displacement (e.g., the first and third rows, the third column in the upper left panel in Figure 8 and the
292 third column in the lower right panel in Figure 8). However, changing the rheological models of the
293 Pro- or Retro-terranes seems to have less impact on the deformation mode of the continental collisional
294 system, according to the simulation results of models which are connected by several cross-shaped
295 solid lines with different colors in Figure 8. Thus, it is difficult to determine whether the horizontal
296 strength contrasts between terranes or the vertical strength variation of a single terrane plays the
297 dominant role in a multi-terrane collisional system. This is also the significance and necessity of our
298 study.

299 **4.2. Influences of Lithosphere Structure**

300 Lithospheric thickness is one of the critical factors that control its strength (Burov, 2011), and it can
301 strongly vary between tectonic regions (Pasyanos et al., 2014). In our models, we assume different
302 lithospheric thicknesses for the Pro-, Mid- and Retro-terrane to explore these effects. Complex effects
303 are seen. When changing the lithospheric thicknesses of the Mid-terrane, or of all three terranes,
304 remarkable variations in lithosphere deformation appear in cases 1 and 2, but smaller variations are
305 seen for cases 3 and 4 (Figure 9). Cases 1 and 2 assume a Jelly sandwich rheology for the Pro-, Mid-
306 and Retro-terrane, so the strength of the lithospheric mantle of three terranes is comparable. Strength
307 variations produced by differences in lithospheric thickness may alter the relative strength of the three

308 terranes, resulting in distinct lithospheric deformations. For example, if the Pro- and Mid-terranes have
309 same lithosphere thickness, deformation mode in Case 2 would change from subduction to thickening
310 (subplot 3 vs. subplot 8 in Figure 9); if the Mid-terrane is thickest or the three terranes have same
311 thickness of lithosphere, deformation mode in Case 1 would change from collision to replacement
312 (subplot 2 vs. subplot 17 and 22 in Figure 9), and the polarity of the subduction of Pro-terrane's
313 lithospheric mantle would be reversed in Case 2 (subplot 3 vs. subplot 18 and 23 in Figure 9). Instead,
314 in cases 3 and 4, the Pro-, Mid- and Retro-terrane have two regions with stronger Jelly-sandwich-like
315 rheological structures and one with a weaker Crème brûlée structure, and deformation preferentially
316 concentrates in the weaker terrane. In comparison to the large strength difference implied for the
317 lithospheric mantle between the Crème brûlée and Jelly Sandwich rheological models, the strength
318 variations associated with the differences in lithosphere thickness are relatively small. Therefore,
319 changing the thicknesses of the lithosphere has much smaller effects on the lithosphere deformation, as
320 seen in cases 3 and 4 (also see the subplots in 3rd and 4th rows of Figure 9).

321 In addition, the weak zones that suture two terranes are generally preserved during continental
322 amalgamation (Burker et al., 1977; Vink et al., 1984; Yin and Harrison, 2000). These local pre-existing
323 lithosphere weaknesses would be preferentially activated if the continental lithosphere were subjected
324 to compression, and could play a key role in concentrating deformation, adjusting deformation
325 sequences, and inducing lithosphere subduction (Sokoutis and Willingshofer, 2011; Heron et al., 2016;
326 Chen et al., 2020; Xie et al., 2021, 2023). Comparing the simulation results of models with and without
327 weak zone, we find that a weak zone will facilitate lithosphere subduction in earlier stages of model
328 evolution, resulting in more diverse lithosphere deformation patterns during the later stage (Figure 10).

329 **4.3. Implications for the Tectonics of East Asia**

330 **4.3.1. Lithosphere Collision beneath the Eastern Tien Shan**

331 The eastern Tien Shan is an ideal region to study the deformation patterns linked to long-term
332 lithosphere collision (Figure 11a). The eastern Tien Shan is bounded by the Tarim Basin to the south,
333 and the Junggar Basin to the north. It is composed of a series of former island arcs and small
334 continental blocks that amalgamated during the late Paleozoic (Han and Zhao, 2017). The lithosphere
335 of the eastern Tien Shan is weaker and thinner in comparison to its neighboring Tarim Basin and
336 Junggar Basin (Kumar et al., 2005; Lei and Zhao et al., 2007; Zhang et al., 2013; Deng and Tesauero,

337 2016). At ~20 – 25 Ma, the eastern Tien Shan became a reactivated orogeny in response to ongoing
338 India-Asia collision (Yin et al., 1998). Compression linked to the India-Asia collision induced the
339 Tarim lithosphere to underthrust northward (Xu et al., 2002; Guo et al., 2006; Lei and Zhao et al., 2007;
340 Lü et al., 2019; Hapaer et al., 2022; Sun et al., 2022). In the northern part of the eastern Tien Shan,
341 significant high-velocity anomalies and Moho overlap are also imaged, which are conventionally
342 explained as being due to the southward underthrusting of the Junggar lithosphere (Xu et al., 2002;
343 Guo et al., 2006; Li et al., 2016; Lü et al., 2019). High-velocity anomalies in the Tarim and Junggar
344 lithosphere appear to connect beneath the eastern Tien Shan, suggesting the lithosphere of the Tarim
345 and Junggar Basins has converged and collided together in this region (Figure 11b; Lü et al., 2019).
346 Bidirectional underthrusting of the Tarim and Junggar lithosphere leads to intense crustal shortening
347 and thrust faults on both flanks over the adjacent basins, as well as attendant fold and reverse fault
348 zones along the range fronts (Yin et al., 1998; Wang et al., 2004).

349 **4.3.2. Lithosphere Thickening and Delamination in the Tibetan Plateau**

350 The deformation pattern arising from lithosphere thickening and delamination has been applied to the
351 Tibetan Plateau (Figure 11c). Tibetan lithosphere may have been significantly weakened by hydration,
352 metasomatism, and partial melting of the lithospheric mantle during a series of oceanic closure and
353 terrane accretion events before the India-Asia collision (Yin and Harrison, 2000; Zhang et al., 2014;
354 Ma et al., 2021). It was then pushed northward by the Indian craton and was blocked by the
355 Tarim/Qaidam craton during India-Asia collision, leading to double crustal thickness (Zhao and
356 Morgan, 1985; Zhang et al., 2011). The lithosphere beneath the Tibetan Plateau does not thicken
357 significantly like its crust, especially beneath northern Tibet (Owens and Zandt, 1997; Tunini et al.,
358 2016). Numerous observations instead suggest that the Tibetan lithosphere has been detached from the
359 crust and has sunk into deeper mantle, consistent with the presence of high-velocity regions in the deep
360 mantle in western, southern and southeastern Tibet (Li et al., 2008; Chen et al., 2017; Feng et al., 2021).
361 A significant depression of the 660-km discontinuity beneath the Himalaya terrane and the uplift of
362 410-km discontinuity in western Tibet have also attributed to the presence of delaminated Tibetan
363 lithosphere (Wu et al., 2022). In northern Tibet, anomalously high temperatures are assumed to be
364 linked to a region of inefficient S_n propagation indicating a thin or absent lithospheric mantle lid in this
365 region, while a remarkable low-velocity zone in the mantle and ultra-potassic volcanics also suggest

366 lithosphere thinning (Barazangi and Ni, 1982; Turner et al., 1996; Owens and Zandt, 1997; Guo et al.,
367 2006; Liang et al., 2012; Tunini et al., 2016). After lithosphere thinning commenced in the Miocene,
368 the Tibetan Plateau rapidly grew outwards (Lu et al., 2018 and references therein; Molnar et al., 1993;
369 Xie et al., 2023).

370 **4.3.3. Lithosphere Subduction in Southeastern China**

371 An example of intracontinental subduction is the Early Paleozoic Orogen in Southeastern China which
372 appears to have not been preceded by oceanic subduction (Figure 11d; Faure et al., 2009). The
373 northeasterly trending Early Paleozoic Orogen of Southeastern China is located on the Wuyi-Yunkai
374 Fold Belt which welds the Cathaysian Block to the south and the Yangtze Block to the north. Two
375 groups of models of collisional belt (Guo et al., 1989; Hsü et al., 1990) and intercontinental orogen
376 (Faure et al., 2009; Charvet et al., 2010; Li et al., 2010) have been proposed to explain the Early
377 Paleozoic Orogen in Southeastern China. Arguments against it being a collisional orogenic belt are its
378 lack of preserved ophiolites, a magmatic arc, subduction complexes, and high-pressure metamorphism;
379 instead, structural, metamorphic, and sedimentary elements indicate that this orogen was an
380 intracontinental orogen controlled by the northward subduction of Cathaysian Block (Faure et al., 2009;
381 Charvet et al., 2010; Li et al., 2010). At ~465 Ma, the Cathaysian Block underthrust beneath the
382 Yangtze Block along the Jiangshan–Shaoxing Fault, in which the lithospheric weaknesses inherited
383 from previous tectonic event of Nanhua rift at 800 – 850 Ma played an important role (Faure et al.,
384 2009; Charvet et al., 2010). During continental subduction, north-south horizontal shortening is
385 accommodated by ductile decollement zones in the Cathaysian Block, causing remarkable
386 south-directed crustal folding and thrusting structures related to both thin-skinned and thick-skinned
387 tectonics in the Wuyishan proper and its southern border, and north-directed structures to the west of
388 Ganjiang Fault and north of Jiangshan–Shaoxing Fault, where only thin-skinned tectonics is visible (Li
389 et al., 1998; Shu et al., 1999; Charvet et al., 2010). The tectonic development of the Early Paleozoic
390 Orogen in Southeastern China appears similar to the deformation mode of lithosphere subduction
391 (Figure 4, 10a and 10c).

392 So far, we have yet to find a suitable region to apply the model deformation pattern of lithosphere
393 replacement. In this deformation pattern, crustal deformation and topographic evolution are similar to
394 those in the deformation pattern of lithosphere collision (Figures 7a and 7c). Thus, it is not easy to

395 identify this pattern by geological and geophysical techniques when the replaced and original
396 continental lithosphere has similar properties. Improved imaging observations with better resolution
397 may allow this deformation pattern to be identified in the future.

398 **5. Model Limitations**

399 Although we can obtain four deformation modes of continental lithosphere by changing the rheologies
400 of different terranes in a collisional model, we must keep in mind that our results are based on some
401 simplifications and assumptions, which may affect the model results. For example, in our model three
402 terranes are directly collaged together, but in nature different terranes are often connected through weak
403 sutures which may preferentially deform when they are subjected to compression (Burker et al., 1977;
404 Yin and Harrison, 2000). These local pre-existing weak zones have non-negligible influences on
405 lithospheric deformation, and their role were widely discussed in previous studies (Sokoutis and
406 Willingshofer, 2011; Heron et al., 2016; Chen et al., 2020 ; Xie et al., 2021, 2023). We also discussed
407 the effects of local pre-existing weak zones in Section 4.2. In addition, lithosphere thicknesses of the
408 Pro-, Mid- and Retro-terrane are chosen arbitrary in our models, but they also have important
409 influences on lithosphere deformation (Figure 9). Some studies suggest that differences in crustal
410 strength will also cause different lithospheric deformation (Faccenda et al., 2008; Vogt et al., 2017,
411 2018), but the three terranes are set same crustal structure in our model for the aim of simplification. As
412 well, some studies believe that the convergence rate will greatly affect the deformation of orogenic
413 belts (Chen et al., 2016; Vogt et al., 2017), but in this study, the impact of the convergence rate is not
414 been discussed.

415 **6. Conclusions**

416 The continental lithosphere is likely to have strong lateral variations in its strength. We explored 2-D
417 numerical models that contain three diverse types of continental terranes to study the responses of
418 continental terranes with different strengths to compression. Four rheological models were respectively
419 applied to each of the Pro-, Mid- and Retro-terrane, and simulation results can be grouped into four
420 distinct deformation styles: lithosphere collision, subduction, thickening and delamination, and
421 replacement. These deformation styles arise from the rheological contrasts between the terranes: (1)

422 when the middle terrane is the weakest, its lithosphere is easily extruded, which leads to lithosphere
423 collision between its two bounding terranes; (2) when the middle terrane has a strong lower crust, while
424 the lower crust of a bounding terrane is weak, then subduction of the lithosphere of the bounding
425 terrane will occur; (3) when a bounding terrane is the weakest, its lithosphere would tend to be
426 thickened by lateral compression, followed by lithosphere delamination due to the resulting
427 density/gravitational instability; (4) when a bounding terrane has a strong lower crust and weak
428 lithospheric mantle, while the middle terrane has a weak lower crust and strong lithospheric mantle,
429 then lithosphere replacement will occur. These simulation patterns are seen in observed deformation
430 patterns and structures in the eastern Tien Shan, and the Tibetan Plateau, the Early Paleozoic Orogen of
431 Southeastern China, suggesting they are likely to be naturally occurring modes of intracontinental
432 orogenesis.

433 ***Code availability***

434 Requests for the numerical code I2VIS should be sent to the main developer
435 (taras.gerya@erdw.ethz.ch).

436 ***Data availability***

437 Numerical modeling data and the model evolution animations of Cases 1 – 4 are all provided in
438 Zenodo (<https://doi.org/10.5281/zenodo.8354366> and <https://doi.org/10.5281/zenodo.10731981>).

439 **Author contribution: Conceptualization:** Yongshun John Chen; **Methodology:** Lin Chen, Renxian
440 Xie; **Investigation:** Renxian Xie; **Formal analysis:** Renxian Xie, Lin Chen; **Visualization:** Renxian
441 Xie, Jason P. Morgan; **Writing – original draft preparation:** Renxian Xie; **Funding acquisition:**
442 Yongshun John Chen, Lin Chen, Renxian Xie.

443 **Competing interests:** The authors declare that they have no conflict of interest.

444 **Disclaimer. Publisher’s note:** Copernicus Publications remains neutral with regard to jurisdictional
445 claims in published maps and institutional affiliations.

446 **Acknowledgments**

447 The authors sincerely thank Prof. Taras Gerya for providing the I2VIS package and his long-lasting
448 guidance on our geodynamic modeling. We are also grateful to the two anonymous reviewers for their
449 insightful comments, which greatly improved the presentation of the paper. The authors acknowledge
450 that figures of simulation results were prepared with the Generic Mapping Tools (GMT,
451 <http://www.soest.hawaii.edu/gmt/>), and the color bar of batlow used in the figures of viscosity field is
452 from Cramer et al. (2018). All models were performed on the TianHe-1A system at the National
453 Supercomputer Center in Tianjin.

454 **Financial support:** This study was supported by the National Natural Science Foundation of China
455 (Grants U1901602), the National Key R&D Program of China (2022YFF0800800) and National
456 Natural Science Foundation of China (42374076).

457 **References**

458 Artemieva, I. M.: Global 1×1 thermal model TC1 for the continental lithosphere: implications for
459 lithosphere secular evolution, *Tectonophysics*, 416, 245-277,
460 <https://doi.org/10.1016/j.tecto.2005.11.022>, 2006.
461 Audet, P., and Bürgmann, R.: Dominant role of tectonic inheritance in supercontinent cycles, *Nature*
462 *geoscience*, 4, 184-187, <https://doi.org/10.1038/ngeo1080>, 2011.

463 Barazangi, M., and Ni, J.: Velocities and propagation characteristics of Pn and Sn beneath the
464 Himalayan arc and Tibetan plateau: Possible evidence for underthrusting of Indian continental
465 lithosphere beneath Tibet, *Geology*, 10, 179-185,
466 [https://doi.org/10.1130/0091-7613\(1982\)10<179:VAPCOP>2.0.CO;2](https://doi.org/10.1130/0091-7613(1982)10<179:VAPCOP>2.0.CO;2), 1982.

467 Bian, S., Gong, J., Chen, L., Zusa, A. V., Chen, H., Lin, X., ... & Yang, R.: Diachronous uplift in
468 intra-continental orogeny: 2D thermo-mechanical modeling of the India-Asia collision,
469 *Tectonophysics*, 775, 228310, <https://doi.org/10.1016/j.tecto.2019.228310>, 2020.

470 Burg, J. P., and Gerya, T. V.: The role of viscous heating in Barrovian metamorphism of collisional
471 orogens: thermomechanical models and application to the Lepontine Dome in the Central Alps,
472 *Journal of Metamorphic Geology*, 23, 75-95, <https://doi.org/10.1111/j.1525-1314.2005.00563.x>,
473 2005.

474 Burke, K., Dewey, J. F., and Kidd, W. S. F.: World distribution of sutures—the sites of former oceans,
475 *Tectonophysics*, 40, 69-99, [https://doi.org/10.1016/0040-1951\(77\)90030-0](https://doi.org/10.1016/0040-1951(77)90030-0), 1977.

476 Burov, E. B., and Watts, A. B.: The long-term strength of continental lithosphere: "jelly sandwich" or "
477 crème brûlée"? *GSA today*, 16, 4, , doi: 10.1130/1052-5173(2006)016<4:tltSOc>2.0.cO;2, 1997,
478 2006.

479 Burov, E. B.: Rheology and strength of the lithosphere, *Marine and petroleum Geology*, 28, 1402-1443,
480 <https://doi.org/10.1016/j.marpetgeo.2011.05.008>, 2011.

481 Bürgmann, R., and Dresen, G.: Rheology of the lower crust and upper mantle: Evidence from rock
482 mechanics, geodesy, and field observations, *Annu. Rev. Earth Planet. Sci.*, 36, 531-567, doi:
483 10.1146/annurev.earth.36.031207.124326, 2008.

484 Charvet, J., Shu, L., Faure, M., Choulet, F., Wang, B., Lu, H., & Le Breton, N.: Structural development
485 of the Lower Paleozoic belt of South China: genesis of an intracontinental orogeny, *Journal of*
486 *Asian Earth Sciences*, 39(4), 309-330, <https://doi.org/10.1016/j.jseaes.2010.03.006>, 2010.

487 Chen, M., Niu, F., Tromp, J., Lenardic, A., Lee, C. T. A., Cao, W., and Ribeiro, J.: Lithospheric
488 foundering and underthrusting imaged beneath Tibet, *Nature communications*, 8, 15659,
489 <https://doi.org/10.1038/ncomms15659>, 2017.

490 Chen, L.: The role of lower crustal rheology in lithospheric delamination during orogeny, *Frontiers in*
491 *Earth Science*, 9, 755519, doi: 10.3389/feart.2021.755519, 2021.

492 Chen, L., Capitanio, F. A., Liu, L., and Gerya, T. V.: Crustal rheology controls on the Tibetan plateau

493 formation during India-Asia convergence, *Nature Communications*, 8, 15992,
494 <https://doi.org/10.1038/ncomms15992>, 2017.

495 Chen, L., & Gerya, T. V.: The role of lateral lithospheric strength heterogeneities in orogenic plateau
496 growth: Insights from 3-D thermo-mechanical modeling, *Journal of Geophysical Research: Solid*
497 *Earth*, 121, 3118–3138, <https://doi.org/10.1002/2016JB012872>. Chen, L., Liu, L., Capitanio, F. A.,
498 Gerya, T. V., and Li, Y.: The role of pre-existing weak zones in the formation of the Himalaya and
499 Tibetan plateau: 3-D thermomechanical modelling, *Geophysical Journal International*, 221,
500 1971-1983, doi: 10.1093/gji/ggaa125, 2020.

501 Chen, W. P., and Molnar, P.: Focal depths of intracontinental and intraplate earthquakes and their
502 implications for the thermal and mechanical properties of the lithosphere, *Journal of Geophysical*
503 *Research: Solid Earth*, 88, 4183-4214, <https://doi.org/10.1029/JB088iB05p04183>, 1983.

504 Chen Y, Morgan W J.: Rift valley/no rift valley transition at mid-ocean ridges, *Journal of Geophysical*
505 *Research: Solid Earth*, 95(B11): 17571-17581, <https://doi.org/10.1029/JB095iB11p17571>, 1990.

506 Cook, K. L., and Royden, L. H.: The role of crustal strength variations in shaping orogenic plateaus,
507 with application to Tibet, *Journal of Geophysical Research: Solid Earth*, 113,
508 <https://doi.org/10.1029/2007JB005457>, 2008.

509 Cramer, F.: Scientific colour maps, Zenodo, 10, 2018, <http://doi.org/10.5281/zenodo.1243862>.

510 Deng, Y., and Tesauro, M.: Lithospheric strength variations in Mainland China: Tectonic implications.
511 *Tectonics*, 35, 2313–2333, <https://doi.org/10.1002/2016TC004272>, 2016.

512 Faccenda, M., Gerya, T. V., and Chakraborty, S.: Styles of post-subduction collisional orogeny:
513 Influence of convergence velocity, crustal rheology and radiogenic heat production, *Lithos*, 103,
514 257-287, <https://doi.org/10.1016/j.lithos.2007.09.009>, 2008.

515 Faure, M., Shu, L., Wang, B., Charvet, J., Choulet, F., and Monie, P.: Intracontinental subduction: a
516 possible mechanism for the Early Palaeozoic Orogen of SE China, *Terra Nova*, 21, 360-368,
517 <https://doi.org/10.1111/j.1365-3121.2009.00888.x>, 2009.

518 Feng, J., Yao, H., Chen, L., and Wang, W.: Massive lithospheric delamination in southeastern Tibet
519 facilitating continental extrusion, *National Science Review*, 9, nwab174, DOI:
520 10.1093/nsr/nwab174, 2022.

521 Gerya, T.: Dynamical instability produces transform faults at mid-ocean ridges, *Science*, 329,
522 1047-1050, DOI: 10.1126/science.1191349, 2010.

523 Gerya, T.: Introduction to numerical geodynamic modelling, 2nd edition, Cambridge University Press,
524 488pp, ISBN: 9781316534243, <https://doi.org/10.1017/9781316534243>, 2019.

525 Gerya, T. V., and Yuen, D. A.: Characteristics-based marker-in-cell method with conservative
526 finite-differences schemes for modeling geological flows with strongly variable transport
527 properties, *Physics of the Earth and Planetary Interiors*, 140, 293-318,
528 <https://doi.org/10.1016/j.pepi.2003.09.006>, 2003a.

529 Gerya, T. V., & Yuen, D. A.: Rayleigh–Taylor instabilities from hydration and melting propel ‘cold
530 plumes’ at subduction zones, *Earth and Planetary Science Letters*, 212(1-2), 47-62,
531 [https://doi.org/10.1016/S0012-821X\(03\)00265-6](https://doi.org/10.1016/S0012-821X(03)00265-6), 2003b.

532 Guo, B., LIU, Q. Y., CHEN, J. H., ZHAO, D. P., LI, S. C., and LAI, Y. G.: Seismic tomography of the
533 crust and upper mantle structure underneath the Chinese Tianshan, *Chinese Journal of Geophysics*,
534 49, 1543-1551, <https://doi.org/10.1002/cjg2.982>, 2006.

535 Guo L.Z., Shi Y.S., Lu H.F., Ma R.S., Dong H.G., & Yang S.F.: The pre-Devonian tectonic patterns and
536 evolution of South China, *Journal of Southeast Asian Earth Sciences*, 3(1-4), 87-93,
537 [https://doi.org/10.1016/0743-9547\(89\)90012-3](https://doi.org/10.1016/0743-9547(89)90012-3), 1989.

538 Hacker, B. R., Kelemen, P. B., and Behn, M. D.: Continental lower crust, *Annual Review of Earth and*
539 *Planetary Sciences*, 43, 167-205, doi: 10.1146/annurev-earth-050212-124117, 2015.

540 Han, Y., and Zhao, G.: Final amalgamation of the Tianshan and Junggar orogenic collage in the
541 southwestern Central Asian Orogenic Belt: Constraints on the closure of the Paleo-Asian Ocean,
542 *Earth-Science Reviews*, 186, 129-152, <https://doi.org/10.1016/j.earscirev.2017.09.012>, 2018.

543 Hapaer, T., Tang, Q., Sun, W., Ao, S., Zhao, L., Hu, J., ... and Xiao, W.: Opposite facing dipping
544 structure in the uppermost mantle beneath the central Tien Shan from Pn travelttime tomography,
545 *International Journal of Earth Sciences*, 111, 2571-2584,
546 <https://doi.org/10.1007/s00531-022-02162-9>, 2022.

547 Heron, P. J., and Pysklywec, R. N.: Inherited structure and coupled crust-mantle lithosphere evolution:
548 Numerical models of Central Australia, *Geophysical Research Letters*, 43, 4962-4970,
549 <https://doi.org/10.1002/2016GL068562>, 2016.

550 Heron, P. J., Pysklywec, R. N., and Stephenson, R.: Lasting mantle scars lead to perennial plate
551 tectonics, *Nature communications*, 7, 11834, <https://doi.org/10.1038/ncomms11834>, 2016.

552 Hsü, K. J., Li, J., Chen, H., Wang, Q., Sun, S., & Şengör, A. M. C.: Tectonics of South China: key to

553 understanding West Pacific geology, *Tectonophysics*, 183(1-4), 9-39,
554 [https://doi.org/10.1016/0040-1951\(90\)90186-C](https://doi.org/10.1016/0040-1951(90)90186-C), 1990.

555 Huangfu, P., Li, Z. H., Gerya, T., Fan, W., Zhang, K. J., Zhang, H., and Shi, Y.: Multi-terrane structure
556 controls the contrasting lithospheric evolution beneath the western and central–eastern Tibetan
557 plateau, *Nature Communications*, 9, 3780, <https://doi.org/10.1038/s41467-018-06233-x>, 2018.

558 Huangfu, P., Li, Z. H., Fan, W., Zhang, K. J., and Shi, Y.: Contrasting collision-induced far-field
559 orogenesis controlled by thermo-rheological properties of the composite terrane, *Gondwana
560 Research*, 103, 404-423, <https://doi.org/10.1016/j.gr.2021.10.020>, 2022.

561 Jackson, J. A.: Strength of the continental lithosphere: time to abandon the jelly sandwich?, *GSA today*,
562 12, 4-10, DOI: 10.1130/1052-5173(2002)012<0004:SOTCLT>2.0.CO;2, 2002.

563 Junmeng, Z., Guodong, L., Zaoxun, L., Xiankang, Z., and Guoze, Z.: Lithospheric structure and
564 dynamic processes of the Tianshan orogenic belt and the Junggar basin, *Tectonophysics*, 376,
565 199-239, <https://doi.org/10.1016/j.tecto.2003.07.001>, 2003.

566 Kelly, S., Butler, J. P., and Beaumont, C.: Continental collision with a sandwiched accreted terrane:
567 Insights into Himalayan–Tibetan lithospheric mantle tectonics?, *Earth and Planetary Science
568 Letters*, 455, 176-195, <https://doi.org/10.1016/j.epsl.2016.08.039>, 2016.

569 Kelly, S., Beaumont, C., and Butler, J. P.: Inherited terrane properties explain enigmatic post-collisional
570 Himalayan-Tibetan evolution, *Geology*, 48, 8-14, <https://doi.org/10.1130/G46701.1>, 2020.

571 Kumar, P., Yuan, X., Kind, R., and Kosarev, G.: The lithosphere-asthenosphere boundary in the Tien
572 Shan-Karakoram region from S receiver functions: Evidence for continental subduction,
573 *Geophysical Research Letters*, 32, <https://doi.org/10.1029/2004GL022291>, 2005.

574 Lei, J., and Zhao, D.: Teleseismic P-wave tomography and the upper mantle structure of the central
575 Tien Shan orogenic belt, *Physics of the Earth and Planetary Interiors*, 162, 165-185,
576 <https://doi.org/10.1016/j.pepi.2007.04.010>, 2007.

577 Li, C., Van der Hilst, R. D., Meltzer, A. S., and Engdahl, E. R.: Subduction of the Indian lithosphere
578 beneath the Tibetan Plateau and Burma, *Earth and Planetary Science Letters*, 274, 157-168,
579 <https://doi.org/10.1016/j.epsl.2008.07.016>, 2008.

580 Li, J., Zhang, J., Zhao, X., Jiang, M., Li, Y., Zhu, Z., ... and Yang, T.: Mantle subduction and uplift of
581 intracontinental mountains: A case study from the Chinese Tianshan Mountains within Eurasia,
582 *Scientific Reports*, 6, 28831, <https://doi.org/10.1038/srep28831>, 2016.

583 Li, Z. H., Liu, M., and Gerya, T.: Lithosphere delamination in continental collisional orogens: A
584 systematic numerical study, *Journal of Geophysical Research: Solid Earth*, 121, 5186-5211,
585 <https://doi.org/10.1002/2016JB013106>, 2016.

586 Li, Z. X.: Tectonic history of the major east Asian lithospheric blocks since the mid - Proterozoic—a
587 synthesis, *Mantle dynamics and plate interactions in East Asia*, 27, 221-243,
588 <https://doi.org/10.1029/GD027p0221>, 1998.

589 Li, Z. X., Li, X. H., Wartho, J. A., Clark, C., Li, W. X., Zhang, C. L., & Bao, C.: Magmatic and
590 metamorphic events during the early Paleozoic Wuyi-Yunkai orogeny, southeastern South China:
591 New age constraints and pressure-temperature conditions, *GSA Bulletin*, 122(5-6), 772-793,
592 <https://doi.org/10.1130/B30021.1>, 2010.

593 Liang, X., Sandvol, E., Chen, Y. J., Hearn, T., Ni, J., Klemperer, S., ... & Tilmann, F.: A complex
594 Tibetan upper mantle: A fragmented Indian slab and no south-verging subduction of Eurasian
595 lithosphere, *Earth and Planetary Science Letters*, 333, 101-111,
596 <https://doi.org/10.1016/j.epsl.2012.03.036>, 2012.

597 Lu, H., Tian, X., Yun, K., and Li, H.: Convective removal of the Tibetan Plateau mantle lithosphere by~
598 26 Ma, *Tectonophysics*, 731, 17-34, <https://doi.org/10.1016/j.tecto.2018.03.006>, 2018.

599 Lü Z., Gao, H., Lei, J., Yang, X., Rathnayaka, S., and Li, C.: Crustal and upper mantle structure of the
600 Tien Shan orogenic belt from full-wave ambient noise tomography, *Journal of Geophysical*
601 *Research: Solid Earth*, 124, 3987-4000, <https://doi.org/10.1029/2019JB017387>, 2019.

602 Ma, L., Wang, Q., Kerr, A. C., and Tang, G. J.: Nature of the pre-collisional lithospheric mantle in
603 central Tibet: Insights to Tibetan Plateau uplift, *Lithos*, 388, 106076,
604 <https://doi.org/10.1016/j.lithos.2021.106076>, 2021.

605 Mitchell, R. N., Zhang, N., Salminen, J., Liu, Y., Spencer, C. J., Steinberger, B., ... and Li, Z. X. : The
606 supercontinent cycle, *Nature Reviews Earth and Environment*, 2, 358-374,
607 <https://doi.org/10.1038/s43017-021-00160-0>, 2021.

608 Molnar, P., England, P., and Martinod, J.: Mantle dynamics, uplift of the Tibetan Plateau, and the Indian
609 monsoon, *Reviews of Geophysics*, 31, 357-396, <https://doi.org/10.1029/93RG02030>, 1993.

610 Morgan J P, Vannucchi P. : Transmogrification of ocean into continent: implications for continental
611 evolution, *Proceedings of the National Academy of Sciences*, 119(15): e2122694119,
612 <https://doi.org/10.1073/pnas.2122694119>, 2022.Owens, T. J., and Zandt, G.: Implications of

613 crustal property variations for models of Tibetan plateau evolution, *Nature*, 387, 37-43,
614 <https://doi.org/10.1038/387037a0>, 1997.

615 Pasyanos, M. E., Masters, T. G., Laske, G., and Ma, Z.: LITHO1. 0: An updated crust and lithospheric
616 model of the Earth, *Journal of Geophysical Research: Solid Earth*, 119, 2153-2173,
617 <https://doi.org/10.1002/2013JB010626>, 2014.

618 Ranalli, G.: *Rheology of the Earth*, 2nd Edition, Springer Science and Business Media, 421pp, ISBN
619 0412546701, 1995.

620 Schmeling, H., Babeyko, A. Y., Enns, A., Faccenna, C., Funicello, F., Gerya, T., ... and Van Hunen, J.:
621 A benchmark comparison of spontaneous subduction models—Towards a free surface, *Physics of
622 the Earth and Planetary Interiors*, 171, 198-223, <https://doi.org/10.1016/j.pepi.2008.06.028>, 2008.

623 Shu L.S., Lu H.F., Jia D.: Study of the ⁴⁰Ar/³⁹Ar Isotopic Age for the Early Paleozoic Tectonothermal
624 Event in the Wuyishan Region, South China, *Journal-Nanjing University Natural Sciences Edition*,
625 35(6), 668-674, 1999.

626 Sokoutis, D., and Willingshofer, E.: Decoupling during continental collision and intra-plate
627 deformation, *Earth and Planetary Science Letters*, 305, 435-444,
628 <https://doi.org/10.1016/j.epsl.2011.03.028>, 2011.

629 Sun, W., Ao, S., Tang, Q., Malusà M. G., Zhao, L., and Xiao, W.: Forced Cenozoic continental
630 subduction of Tarim craton-like lithosphere below the Tianshan revealed by ambient noise
631 tomography, *Geology*, 50, 1393-1397, <https://doi.org/10.1130/G50510.1>, 2022.

632 Sun, Y., and Liu, M.: Rheological control of lateral growth of the Tibetan Plateau: Numerical results,
633 *Journal of Geophysical Research: Solid Earth*, 123, 10-124,
634 <https://doi.org/10.1029/2018JB016601>, 2018.

635 Tunini, L., Jimenez-Munt, I., Fernandez, M., Verges, J., Villasenor, A., Melchiorre, M., and Afonso, J.
636 C.: Geophysical-petrological model of the crust and upper mantle in the India-Eurasia collision
637 zone, *Tectonics*, 35, 1642–1669, <https://doi.org/10.1002/2016TC004161>, 2016.

638 Turner, S., Arnaud, N., Liu, J., Rogers, N., Hawkesworth, C., Harris, N., ... and Deng, W.:
639 Post-collision, shoshonitic volcanism on the Tibetan Plateau: implications for convective thinning
640 of the lithosphere and the source of ocean island basalts, *Journal of petrology*, 37, 45-71,
641 <https://doi.org/10.1093/petrology/37.1.45>, 1996.

642 Vink G E, Morgan W J, Zhao W L: Preferential rifting of continents: a source of displaced terranes[J].

643 Journal of Geophysical Research: Solid Earth, 89(B12): 10072-10076,
644 <https://doi.org/10.1029/JB089iB12p10072>, 1984.

645 Vogt, K., Matenco, L., and Cloetingh, S.: Crustal mechanics control the geometry of mountain belts.
646 Insights from numerical modelling, *Earth and Planetary Science Letters*, 460, 12-21,
647 <https://doi.org/10.1016/j.epsl.2016.11.016>, 2017.

648 Vogt, K., Willingshofer, E., Matenco, L., Sokoutis, D., Gerya, T., and Cloetingh, S.: The role of lateral
649 strength contrasts in orogenesis: A 2D numerical study, *Tectonophysics*, 746, 549-561,
650 <https://doi.org/10.1016/j.tecto.2017.08.010>, 2018.

651 Wang, C. Y., Yang, Z. E., Luo, H., and Mooney, W. D.: Crustal structure of the northern margin of the
652 eastern Tien Shan, China, and its tectonic implications for the 1906 M~7.7 Manas earthquake,
653 *Earth and Planetary Science Letters*, 223, 187-202, <https://doi.org/10.1016/j.epsl.2004.04.015>,
654 2004.

655 Wang, M., and Shen, Z. K.: Present-day crustal deformation of continental China derived from GPS
656 and its tectonic implications, *Journal of Geophysical Research: Solid Earth*, 125, e2019JB018774,
657 <https://doi.org/10.1029/2019JB018774>, 2020.

658 Wu, Y., Bao, X., Zhang, B., Xu, Y., and Yang, W.: Seismic evidence for stepwise lithospheric
659 delamination beneath the Tibetan Plateau, *Geophysical Research Letters*, 49, e2022GL098528,
660 <https://doi.org/10.1029/2022GL098528>, 2022.

661 Xie, R., Chen, L., Xiong, X., Wang, K., and Yan, Z.: The Role of Pre-existing Crustal Weaknesses in
662 the Uplift of the Eastern Tibetan Plateau: 2D Thermo-Mechanical Modeling, *Tectonics*, 40,
663 e2020TC006444, <https://doi.org/10.1029/2020TC006444>, 2021.

664 Xie, R., Chen, L., Yin, A., Xiong, X., Chen, Y. J., Guo, Z., and Wang, K.: Two phases of crustal
665 shortening in northeastern Tibet as a result of a stronger Qaidam lithosphere during the Cenozoic
666 India–Asia collision, *Tectonics*, 42, e2022TC007261, <https://doi.org/10.1029/2022TC007261>,
667 2023.

668 Xu, Y., Liu, F., Liu, J., and Chen, H.: Crust and upper mantle structure beneath western China from P
669 wave travel time tomography, *Journal of Geophysical Research: Solid Earth*, 107, ESE-4,
670 <https://doi.org/10.1029/2001JB000402>, 2002.

671 Yin, A., Nie, S., Craig, P., Harrison, T. M., Ryerson, F. J., Xianglin, Q., and Geng, Y.: Late Cenozoic
672 tectonic evolution of the southern Chinese Tian Shan, *Tectonics*, 17, 1-27,

673 <https://doi.org/10.1029/97TC03140>, 1998.

674 Yin, A., and Harrison, T. M.: Geologic evolution of the Himalayan-Tibetan orogen, Annual review of
675 earth and planetary sciences, 28, 211-280, <https://doi.org/10.1146/annurev.earth.28.1.211>, 2000.

676 Zhang, Z., Deng, Y., Teng, J., Wang, C., Gao, R., Chen, Y., and Fan, W.: An overview of the crustal
677 structure of the Tibetan plateau after 35 years of deep seismic soundings, Journal of Asian Earth
678 Sciences, 40, 977-989, <https://doi.org/10.1016/j.jseaes.2010.03.010>, 2011.

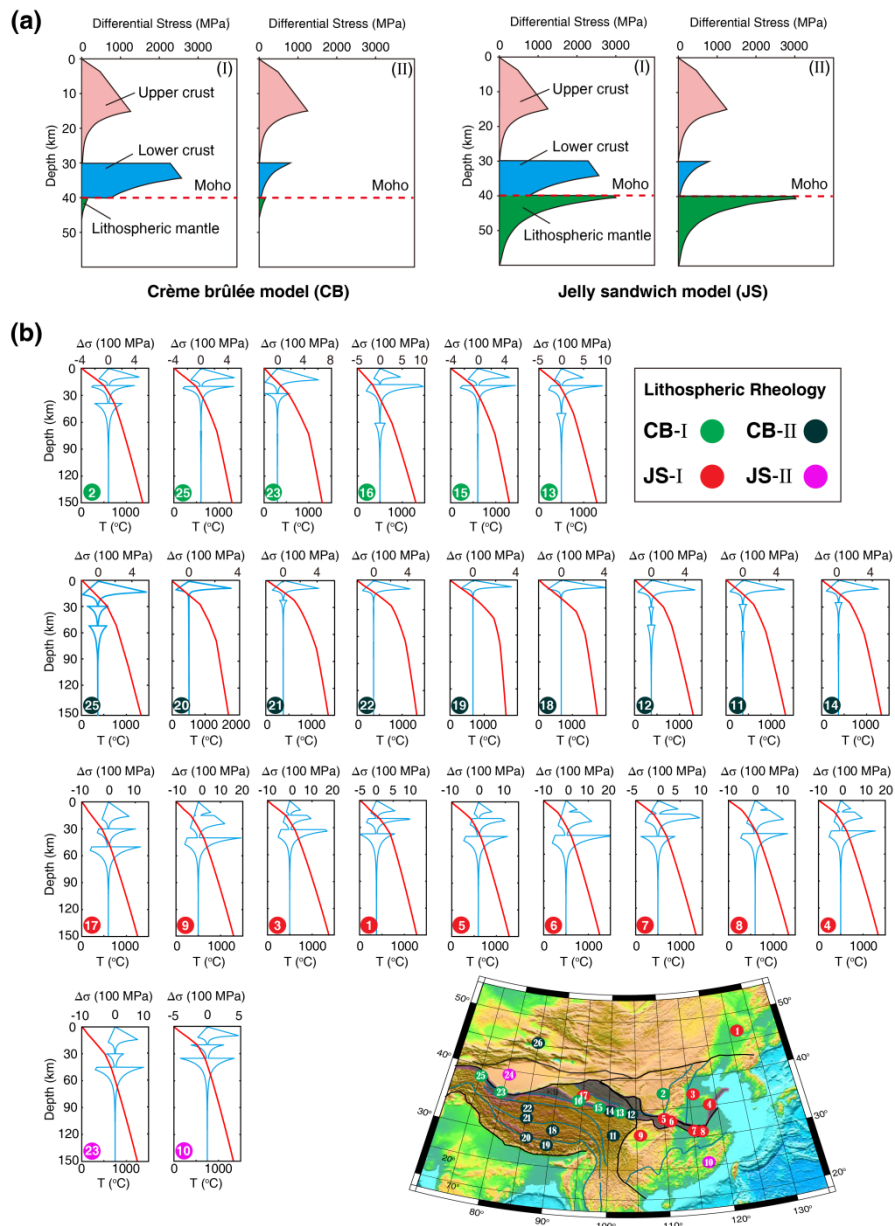
679 Zhang, Z., Deng, Y., Chen, L., Wu, J., Teng, J., and Panza, G.: Seismic structure and rheology of the
680 crust under mainland China, Gondwana Research, 23, 1455-1483,
681 <https://doi.org/10.1016/j.gr.2012.07.010>, 2013.

682 Zhang, Z., Teng, J., Romanelli, F., Braitenberg, C., Ding, Z., Zhang, X., ... & Panza, G. F.: Geophysical
683 constraints on the link between cratonization and orogeny: Evidence from the Tibetan Plateau and
684 the North China Craton. Earth-Science Reviews, 130, 1-48,
685 <https://doi.org/10.1016/j.earscirev.2013.12.005>, 2014.

686 Zhao W L, Morgan W J.: Uplift of Tibetan plateau, Tectonics, 4(4),
687 359-369, <https://doi.org/10.1029/TC004i004p00359>, 1985.

688

689



691

692 **Figure 1. Four rheological models of continental lithosphere.** (a) Crème brûlée model (CB) and Jelly sandwich

693 model (JS). The two rheological models can be further subdivided into CB-I, CB-II, JS-I, and JS-II according to

694 the strength of the lower crust (modified from Jackson, 2002). (b) Observations of four distinct lithosphere

695 rheological structures implied for East Asia (modified from Zhang et al., 2013). Locations of strength profiles are

696 pointed out by dots with numbers in the topography map. Dots filled with different colors indicate different models

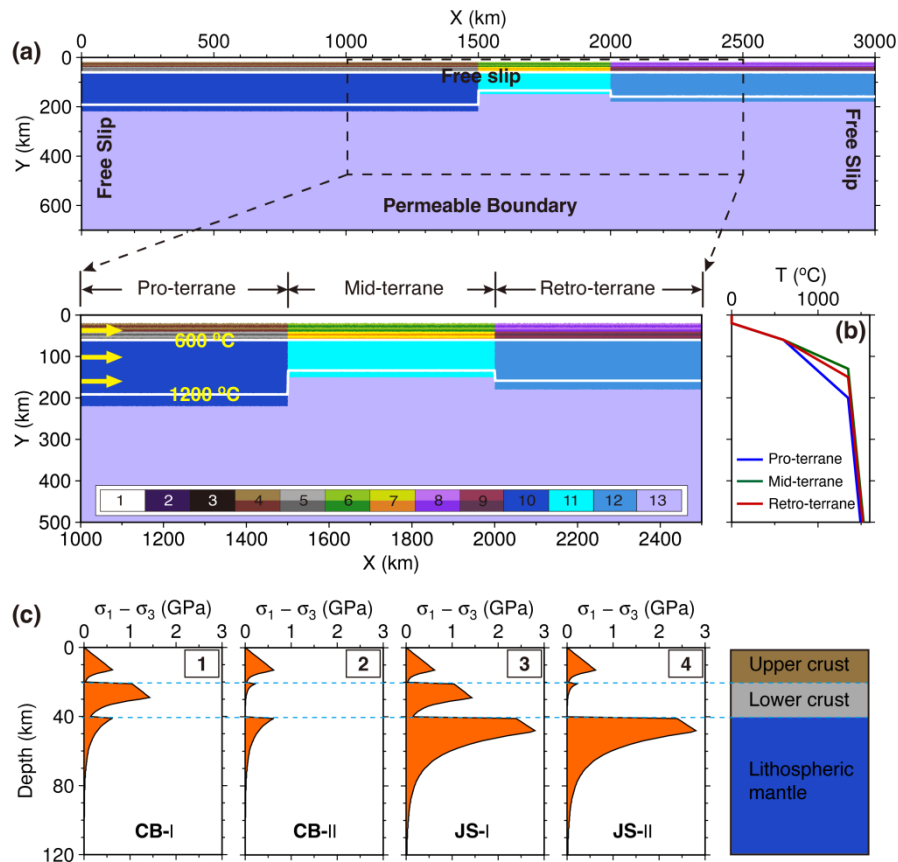
697 of lithospheric rheology. These strength profiles are calculated based on observed geothermal structure and

698 lithospheric structure, and assumed that compositions of the upper and lower crust and lithospheric mantle are wet

699 quartzite, undried granulite and dry olivine, respectively. Variations of temperature and lithospheric compositions

700 lead to a diverse suite of strength profiles vs. depth.

701



702

703 **Figure 2. Initial model setup.** (a) Initial model configuration. The model size is 3000 km × 700 km, and size of

704 study region is 1500 km × 500 km. Three continental terranes of the Pro-, Mid- and Retro-terrane are contained

705 in the numerical model, and they are 200 km, 130 km, and 160 km thick, respectively. White lines are isotherms

706 with an interval of 600 °C. Yellow arrows indicate the convergence rate of 20 mm/yr. Colored grids: 1 – sticky air;

707 2 – sediments; 3 – weak zone; 4, 6, 8 – the upper crust of the Pro-, Mid- and Retro-terrane, respectively; 5, 7, 9 –

708 the lower crust of the Pro-, Mid- and Retro-terrane, respectively; 10, 11, 12 –lithospheric mantle of the Pro-,

709 Mid- and Retro-terrane, respectively; 13 – asthenosphere. (b) Initial temperature structure for the three terranes.

710 The Pro- and Mid-terrane respectively have a coldest and warmest lithospheric mantle due to their differences of

711 lithosphere thicknesses. (c) Four rheological models with contrasting lithospheric strength profiles. These are

712 derived from different strength scaling factor (S) combinations for the upper crust, lower crust, and lithospheric

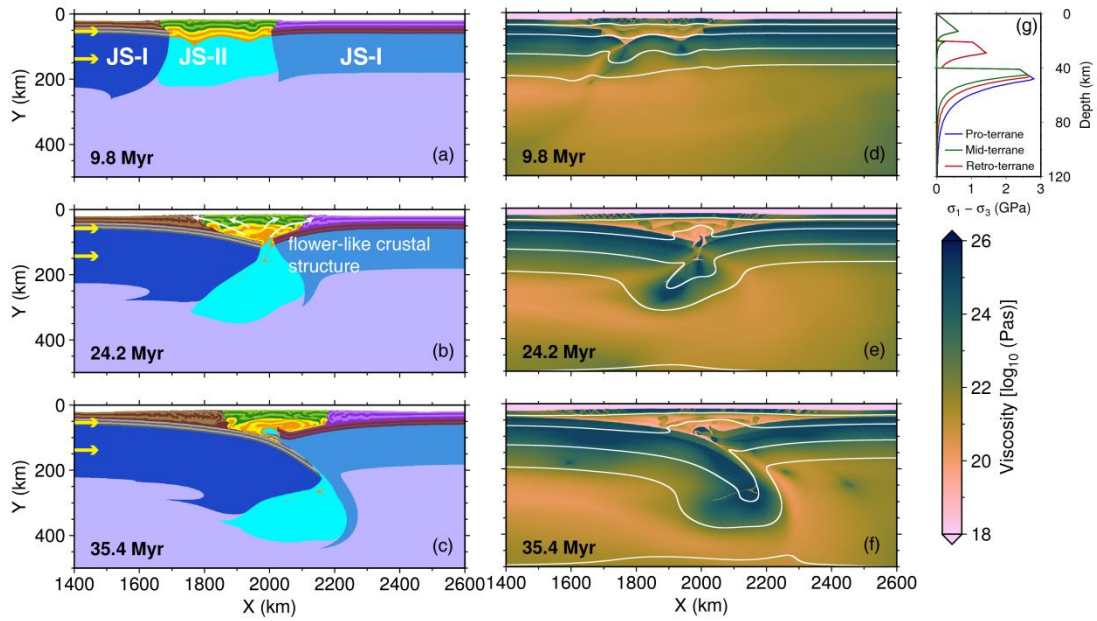
713 mantle (Table S1). Strength profiles are calculated based on the Pro-terrane's initial lithospheric structure,

714 composition, and temperature field. The prescribed strain rate is $1 \times 10^{-14} \text{ s}^{-1}$. CB-I and CB-II, the crème brûlée

715 model with strong and weak lower crust, respectively; JS-I and JS-II, the jelly sandwich model with strong and

716 weak lower crust, respectively.

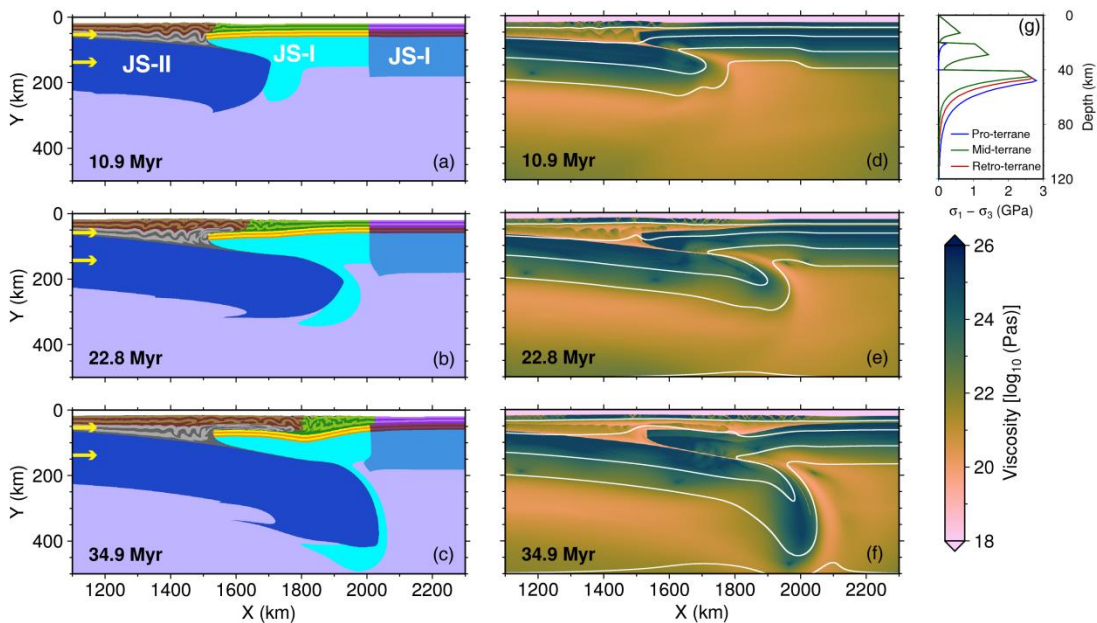
717



718

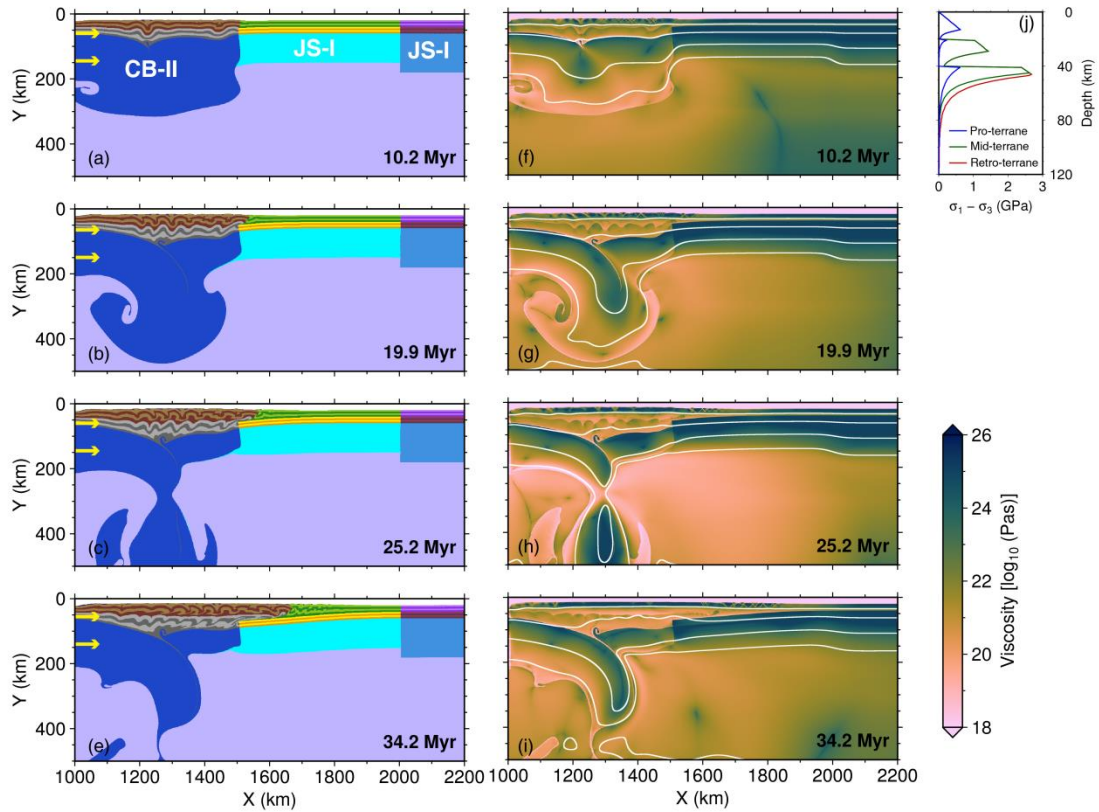
719 **Figure 3. Collision of the lithospheres of the Pro- and Retro-terranes.** Rheological models for the Pro-, Mid- and
 720 Retro-terranes are JS-I, JS-II, and JS-I, respectively, as shown in (g). The left panel shows compositional
 721 fields at 9.8 Myr, 24.2 Myr, and 35.4 Myr, respectively. Yellow arrows indicate the convergence rate. The right
 722 panel shows the corresponding viscosities. White lines are isotherms with an interval of 300 °C.

723



724

725 **Figure 4. Subduction of the lithosphere of the Pro-terrane.** Rheological models for the Pro-, Mid- and
 726 Retro-terranes are JS-II, JS-I, and JS-I, respectively. See Figure 3 for plotting conventions.

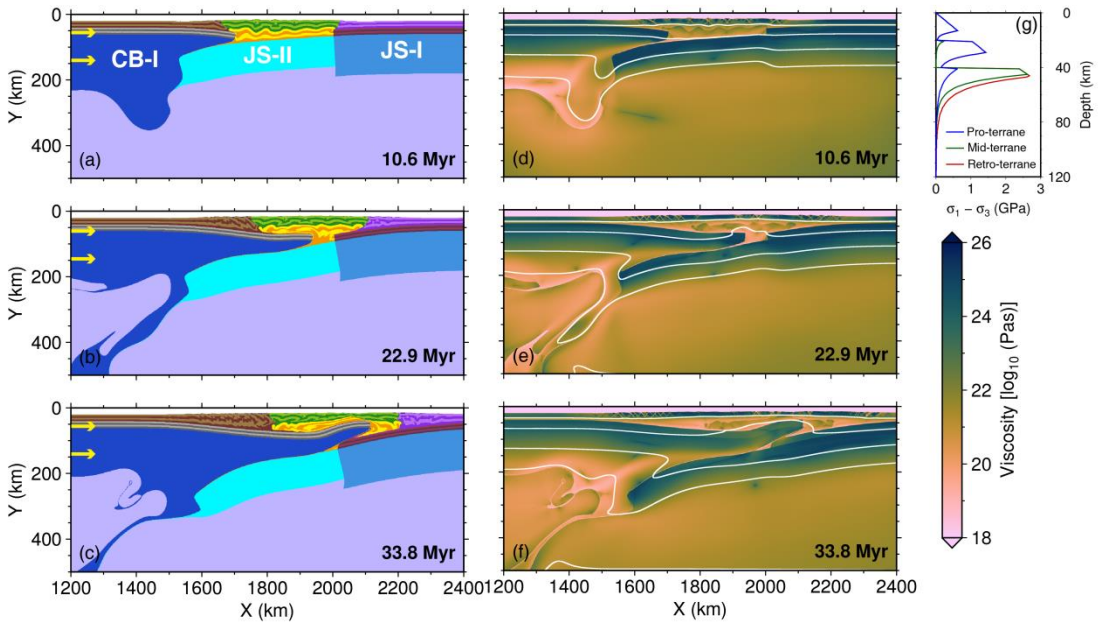


728

729 **Figure 5. Thickening and delamination of the lithosphere of the Pro-terrane.** Rheological models for the Pro-,

730 Mid- and Retro-terrane are CB-II, JS-I, and JS-I, respectively. See Figure 3 for plotting conventions.

731

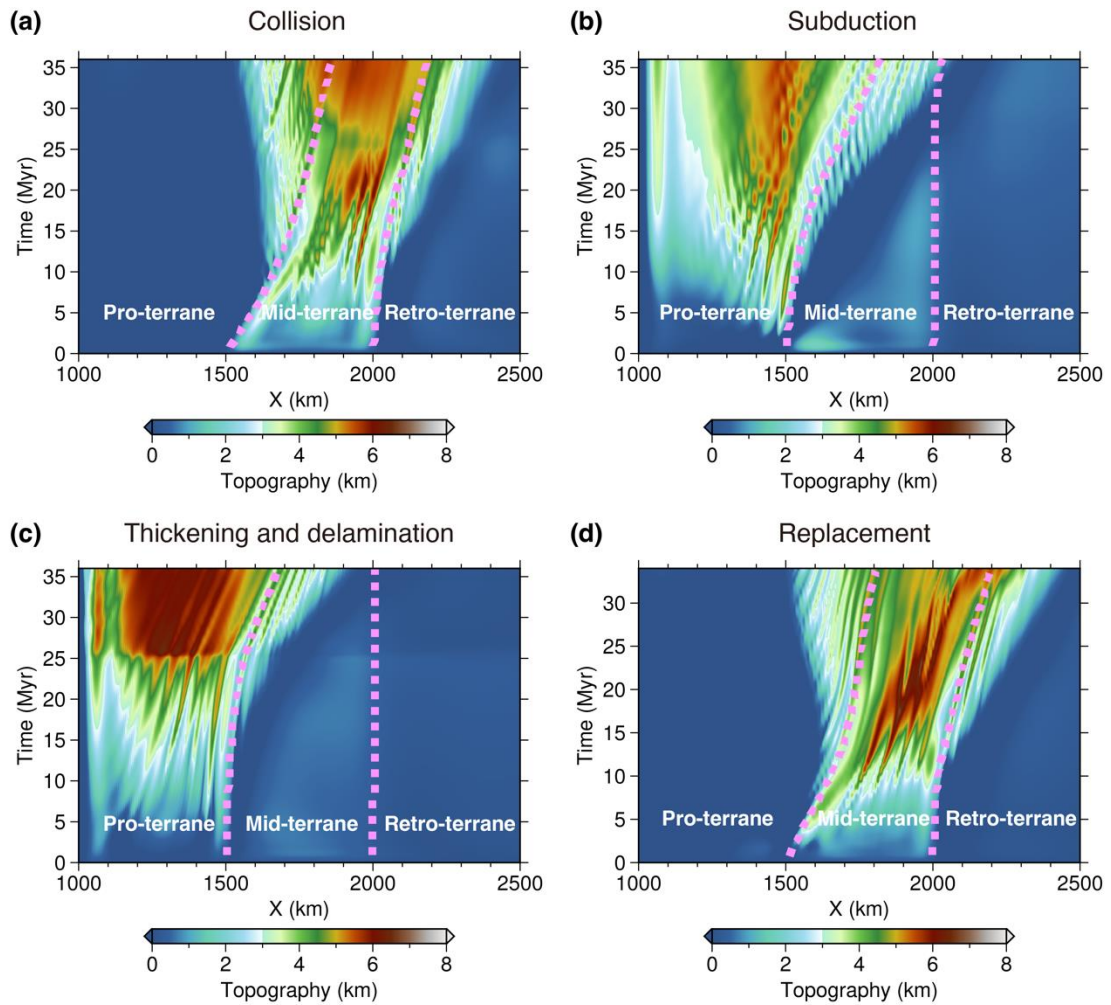


732

733 **Figure 6. Replacement of the lithosphere of the Pro-terrane.** Rheological models for the Pro-, Mid- and

734 Retro-terrane is CB-I, JS-II, and JS-I, respectively. See Figure 3 for plotting conventions.

735



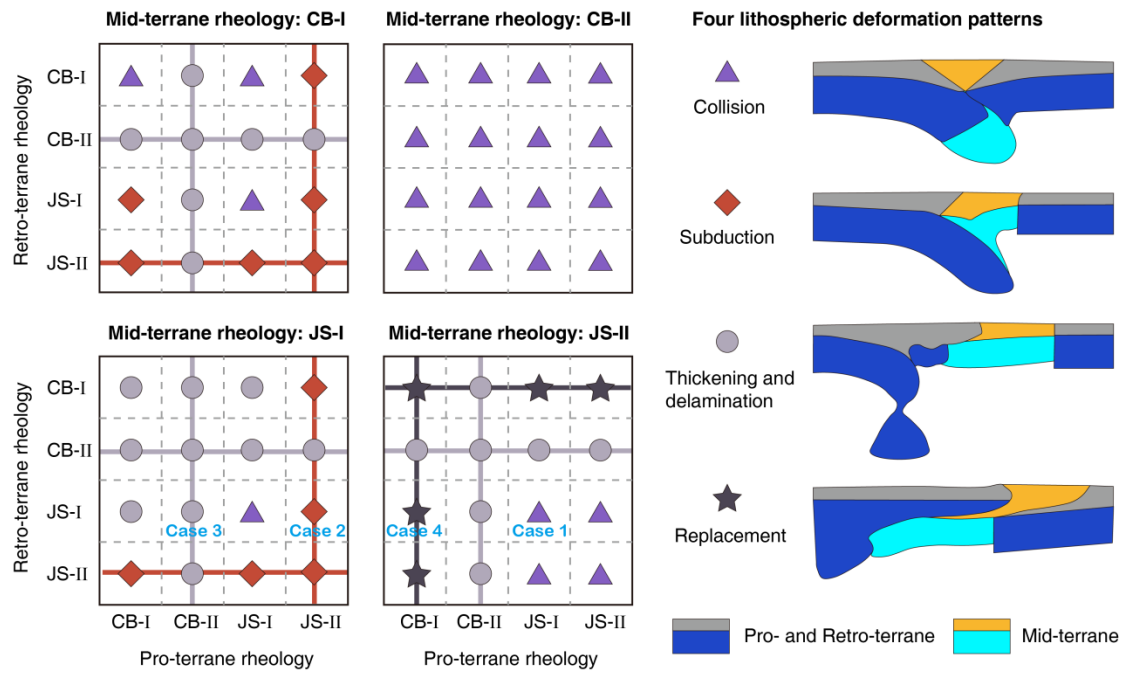
736

737 **Figure 7. Evolution of surface relief for the different deformation styles.** The purple dashed lines indicate the

738 boundaries between terranes. (a) – (d) Surface relief associated with the deformation patterns of lithosphere

739 collision, subduction, thickening and delamination, and replacement, respectively.

740



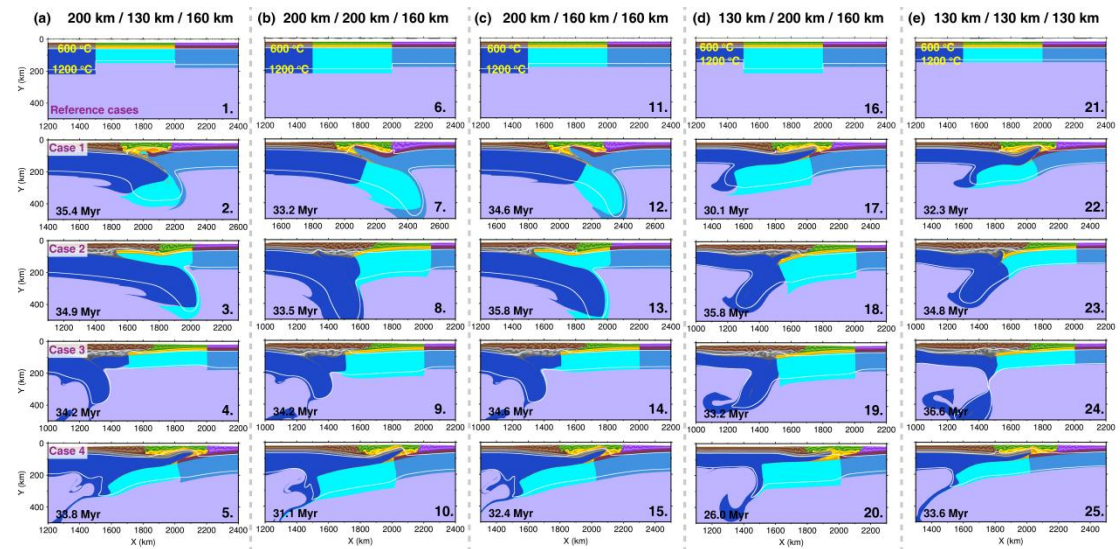
741

742 **Figure 8. Four styles of lithosphere deformation patterns.** Symbols with colors indicate different deformation

743 patterns of the lithosphere. Cases 1 – 4 are the selected models chosen to illustrate details of these modes of

744 compressional evolution.

745



746

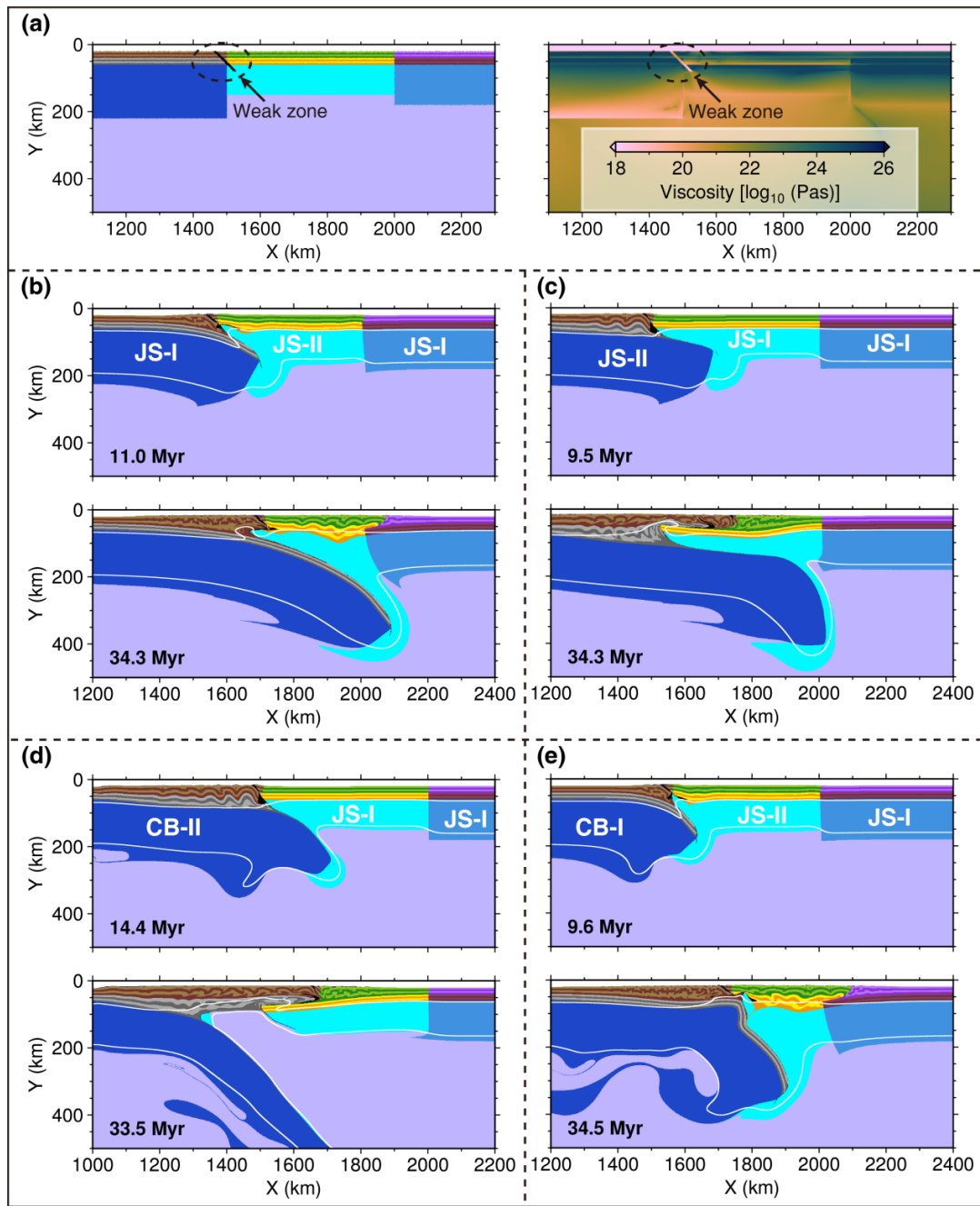
747 **Figure 9. Effects of lithosphere thicknesses of various terranes.** (a) – (e) Final simulation results of models with

748 the different lithosphere thicknesses of the Pro-, Mid-, and Retro-terranes, respectively. (a) Final simulation

749 results of reference cases. Rheological models of the Pro-, Mid- and Retro-terranes in 2 – 4 rows are same with

750 those in Cases 1 – 4, respectively.

751

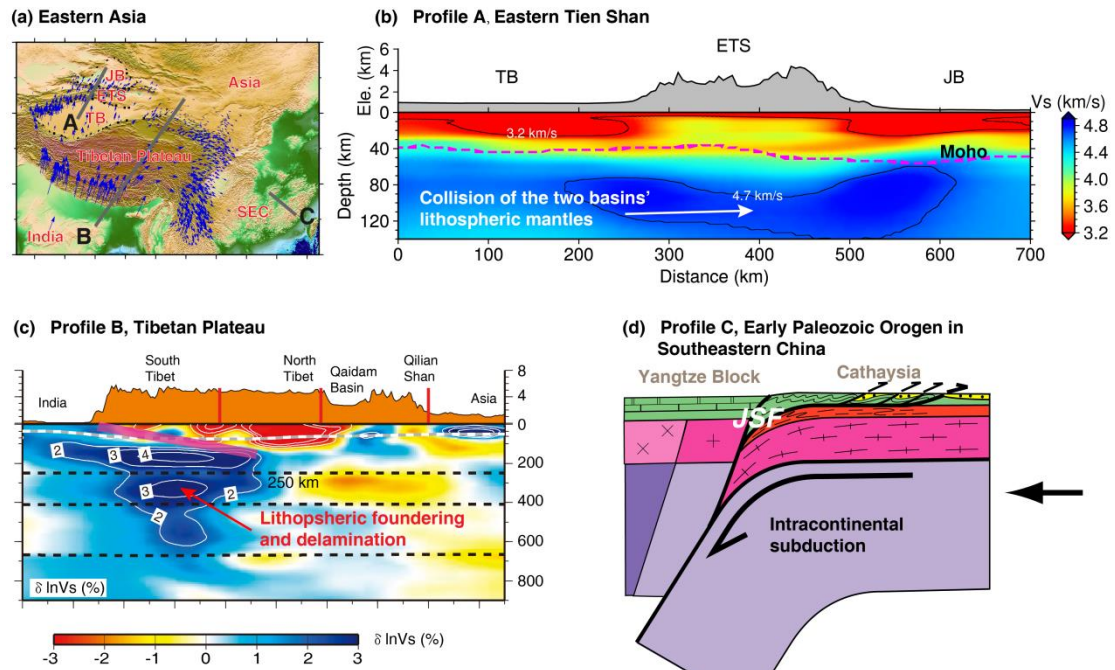


752

753 **Figure 10. Effects of local weak zone on lithosphere deformation.** (a) Details about the weak zone. (b) – (e)

754 Final simulation results of models corresponding to Cases 1 – 4, respectively.

755



756

757 **Figure 11. Implications of simulation results to East Asia.** (a) Topography of East Asia. The three gray lines

758 point out the locations of lithosphere profiles in (b), (c) and (d). TB, Tarim Basin; ETS, eastern Tien Shan; JB,

759 Junggar Basin; SEC, Southeastern China. (b) Collision of the lithospheric mantle of Tarim Basin and Junggar

760 Basin beneath the eastern Tien Shan (modified from Lü et al., 2019). (c) Lithospheric founding and delamination

761 in the Tibetan Plateau (modified from Chen et al., 2017). (d) Intracontinental subduction in the Early Paleozoic

762 Orogen in southeastern China (modified from Faure et al., 2009). JSF, Jiangshan–Shaoxing Fault.

763 **Table 1. Flow laws and material properties for different lithospheric layers.** ρ_0 is the initial density; it evolves

764 with time as $\rho = \rho_0 (1 - \alpha(T - T_0))(1 + \beta(P - P_0))$, where $T_0 = 20^\circ\text{C}$, $P_0 = 10^5$ MPa. Flow law: qtz. = quartzite, Plag.

765 = plagioclase, ol. = olivine.

Material properties	Sediment	Upper crust	Lower crust	Lithospheric mantle	Asthenosphere
ρ_0 (kg/m ³)	2600	2700	2800	3300	3300
Flow laws	Wet qtz.	Wet qtz.	Plag.	Dry ol.	Dry ol.
$1/A_D$ (Pa ⁿ s)	1.97×10^{17}	1.97×10^{17}	4.80×10^{22}	3.98×10^{16}	3.98×10^{16}
n	2.3	2.3	3.2	3.5	3.5
E_a (KJ/mol)	154	154	238	532	532
V_a (J/bar)	0.8	0.8	1.2	1.2	1.2
$\phi = \sin(\varphi)$	0.2 – 0.1	0.3 – 0.1	0.3 – 0.1	0.6 – 0.4	0.6 – 0.3
C (Pa)	$1 \times 10^{7-6}$	$1 \times 10^{7-6}$	$1 \times 10^{7-6}$	$1 \times 10^{7-6}$	$1 \times 10^{7-6}$
H_r (uW/m ³)	2.0	1.5	0.5	0.022	0.022
C_p (J/kg K)	1000	1000	1000	1000	1000
α (1/K)	3×10^{-5}	3×10^{-5}	3×10^{-5}	3×10^{-5}	3×10^{-5}
β (1/MPa)	1×10^{-5}	1×10^{-5}	1×10^{-5}	1×10^{-5}	1×10^{-5}
k (W/m/K)	$0.64 + 807/(T+77)$	$0.64 + 807/(T+77)$	$1.18 + 474/(T+77)$	$[0.73 + 1293/(T+77)] \times (1 + 0.00004P)$	$[0.73 + 1293/(T+77)] \times (1 + 0.00004)$

766